Mechanical Characterization of Nanocrystalline Materials via a Finite Element Nanoindentation Model

Konstantinos Tserpes [1],*[ID], **Panagiotis Bazios** [1][ID], **Spiros G. Pantelakis** [1], **Maria Pappa** [2][ID] **and Nikolaos Michailidis** [2][ID]

1 Laboratory of Technology & Strength of Materials, Department of Mechanical Engineering & Aeronautics, University of Patras, 26500 Patras, Greece; pbazios@upatras.gr (P.B.); pantelak@mech.upatras.gr (S.G.P.)
2 Physical Metallurgy Laboratory, Mechanical Engineering Department, School of Engineering, Aristotle University of Thessaloniki, 54124 Thessaloniki, Greece; pappmari@auth.gr (M.P.); nmichail@auth.gr (N.M.)
* Correspondence: kitserpes@upatras.gr; Tel.: +30-261-096-9498

Abstract: The difficulty of producing sufficient quantities of nanocrystalline materials for test specimens has led to an effort to explore alternative means for the mechanical characterization of small material volumes. In the present work, a numerical model simulating a nanoindentation test was developed using Abaqus software. In order to implement the model, the principal material properties were used. The numerical nanoindentation results were converted to stress–strain curves through an inverse algorithm in order to obtain the macroscopic mechanical properties. For the validation of the developed model, nanoindentation tests were carried out in accordance with the ISO 14577. The composition of 75% wt. tungsten and 25% wt. copper was investigated by producing two batches of specimens with a coarse-grain microstructure with an average grain size of 150 nm and a nanocrystalline microstructure with a grain diameter of 100 nm, respectively. The porosity of both batches was derived to range between 9% and 10% based on X-ray diffraction analyses. The experimental nanoidentation results in terms of load–displacement curves show a good agreement with the numerical nanoindentation results. The proposed numerical technique combined with the inverse algorithm predicts the material properties of a fully dense, nanocrystalline material with very good accuracy, but it shows an appreciable deviation with the corresponding compression results, leading to the finding that the porosity effect is a crucial parameter which needs to be taken into account in the multiscale numerical methodology.

Keywords: nanocrystalline materials; finite element analysis; inverse algorithm

1. Introduction

Notable attempts have been made, in recent years, at the production of materials with a nanocrystalline microstructure, due to their improved mechanical properties [1,2]. The enhancement in terms of strength by decreasing the grain size has been described by the Hall-Petch equation effect [3].

Various manufacturing methods are applied to obtain nanocrystalline alloys (i.e., a grain size less than 100 nm), including electrodeposition [1,4], powder metallurgy [5,6], magnetron sputtering [7–10], and inert gas condensation followed by the consolidation of powders [1] and severe plastic deformation (SPD) [11,12]. The vast majority of nanocrystalline materials are produced by the mechanical alloying method or electrodeposition technique. The electrodeposition technique has some inherent limitations in terms of the quality of the produced specimens because they show extensive porosity or impurities. On the other hand, the fabrication technique of mechanical alloying is able to produce materials with a nanocrystalline microstructure at a high manufacturing speed and with complete control of the fabrication parameters, so as to obtain defect-free bulk materials [13]. However, the main obstacle of the mechanical alloying method is the production of specimens without a uniform grain size, which in turn influences the macroscopic

mechanical response of the materials, especially in a harsh environment. The material microstructure changes rapidly at elevated temperatures. This is the commonly-known coarsening effect. The mechanical response of said materials is completely influenced by their different interphases into the microstructure. This kind of material is the so-called graded material [14,15].

Taking for granted said facts, all of the proposed production techniques are cost-effective, but the produced materials are influenced by several imperfections (like flaws and pores) which drive to the degradation of the material properties. With respect to limitations in the manufacturing methods of nano-crystalline materials, the mass production of fully dense, bulk forms with a nanocrystalline microstructure at sufficient quantities has hardly been achievable up to now, and it has not been industrialized.

With the aforementioned increasing interest in the production of innovative metallic materials, mechanical testing procedures using small material volumes are more than necessary nowadays. Moreover, the conventional testing techniques like tensile or compression testing become noticeably challenging with specimens of small volume. Furthermore, limited results are shown in journals concerning the correlation between the microstructure and the resulting material properties. Some of the desirable material properties in the frame of nanocrystalline materials are the yield stress, the ultimate strength at fracture, the enhanced wear resistance and the improved plasticity compared to that of their microcrystalline counterparts [16–20]. A more detailed and extensive mechanical characterization is needed so as to obtain more reliable results.

Based on the obstacles of the mechanical characterization utilizing conventional experimental tests, scientific progress has resulted in the extensive use of nanoindentation experiments [21–34]. Berkovich indenters allow precise measurements by varying the force of the nanoindentation (P) in relation to the depth of penetration (h). Observations through experimental nanoindentation tests were performed on many materials so as to determine material features such as residual stresses and hardness [23–25,29,33–37].

At the same time, a noticeable effort has been made to use analytical and numerical investigations in order to determine the deformation mechanisms and the contact mechanics of the nanoindentation effect. The main purpose is to define the mechanical response to the applied load of nanoindentation (P) versus penetration depth (h) diagrams acquired from instrumented nanoindentation [23,25,31,32,36–41]. More specifically, researchers [23,25] suggested analytical approaches in which the modulus of elasticity and hardness could be extracted from the P_{max} and the unloading incline at the starting stages. Additionally, Giannakopoulos and Suresh [40] proposed a procedure in which all of elastoplastic properties may be extracted through a *P-h* diagram. Based on [40], Suresh and Giannakopoulos [42] developed an up-to-date methodology which was able to export the residual stresses. In terms of numerical methods, several numerical attempts were conducted on the case studies of thin-film systems [43–45].

To conclude, a methodology was developed by Hill et al. [46] for the case study of materials with power law plastic behavior under the indentation load of a spherical indenter. The calculations of a sharp indenter, such as a Berkovich indenter, for the case of elastoplastic materials were numerically extracted by Larsson et al. [47] and Giannakopoulos et al. [38]. Moreover, scale factors were carried out so as to investigate bulk materials [31,32,39] and coated material [45]. To this end, researchers [32] have developed a comprehensive analytical approach, and several investigations were conducted on the basis of the dimensional analysis of sharp indentation. The results from the aforementioned approach showed that Kick's Law is a constitutive factor of the dimensional analysis of sharp indentation.

The scope of the present paper is to develop an innovative multiscale finite element methodology simulating the nanoindentation test which accounts for the different material phases, as they are described in [48], in order to define the macroscopic mechanical response of nanocrystalline materials. Through the aforementioned model, the nanoindentation behavior of nanocrystalline materials was extracted, and the corresponding macroscopic

mechanical behavior was evaluated via the implementation of an inverse analytical algorithm. By utilizing a homogenized RVE for the last simulation in conjunction with the inverse algorithm, we are able to predict the macroscopic mechanical response.

2. Modelling

2.1. Analytical Approach

As referred to above, the nanoindentation method is a very attractive testing procedure to obtain the mechanical properties of such kinds of materials as nanocrystalline metals, which are difficult to produce in large quantities, leading to the need for the mechanical characterization of small-volume specimens. The uniqueness of the nanoindentation technique relies on the extracted results which come from the *P-h* diagram. More specifically, the estimation of the contact pressure between the nano-indenter and the target material—and the resulting hardness—comes from the measurement of the contact area between said parts in terms of the indentation load and penetration depth. A continuous data acquisition in the loading phase of a typical indentation test is involved. In the following unloading part of the *P-h* diagram, the Young's modulus and Poisson ratio of the indented material can be exported at the early stages of the unloading phase because of the strain relaxation within the material [49,50]. Furthermore, material features like residual stress [46,51], initial plasticity [51–53], creep [54], and hardening [55] are very important parameters for property extraction in the nanoindentation testing method. Additionally, the surface deformation around the plastic deformation induced by the nano-indenter creates sink-in and pile-up residual strains, which are very important for the mechanical characterization of the target material [56]. The aforementioned alteration of the surface plays an important role in determining the contact area, and is also an effective factor for the definition of material properties like the strain-hardening behavior [57,58].

According to the literature for the indentation testing method, a nanoindentation test is commonly known for the creation of a non-uniform stress field at the surface of the target material, which leads to the average calculation of induced stresses [59]. The mean value of stresses in terms of von Mises stress, according to Meyer's hardness [49,59], is defined utilizing the Tabor Relation [59–61]:

$$\sigma \approx \frac{H}{3}, \tag{1}$$

$$H = \frac{P}{A}, \tag{2}$$

where *H* is the resulting hardness, *P* is the applied force of the nano-indenter on the target material, and *A* is the contact area of the Berkovich nanoindenter. The indentation area is calculated taking into consideration the geometry of the nanoindenter's tip and the pileup or sink-in that take place around the tip, as shown in Figure 1.
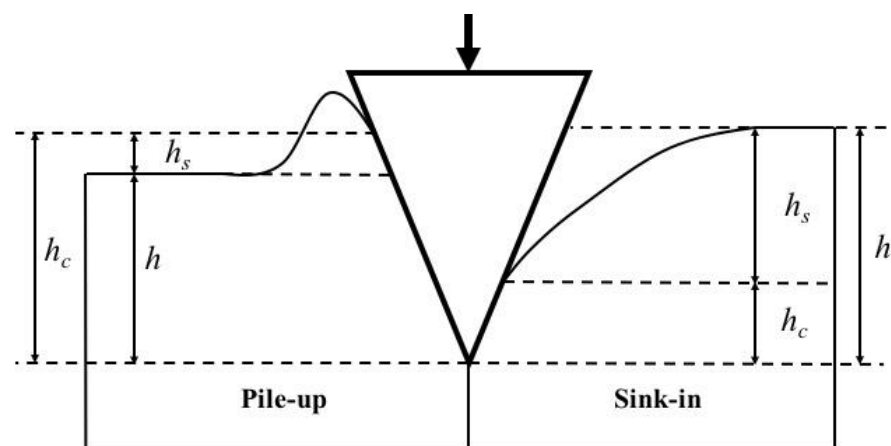

Figure 1. Indentation geometry showing the pile-up and sink-in.

The mathematical expressions followed for the calculation of the projected contact area of the nanoindenter are presented in Equation (3) for the case study of a Berkovich indenter's tip [62], and in Equation (4) for the case study of the spherical indenter's tip:

$$A = 24.5h_c{}^2 + Ch_c,\qquad(3)$$

$$A = \pi\left(2Rh_c - h_c{}^2\right),\qquad(4)$$

where h_c is the penetration depth of the indenter tip into the target specimen, C is a constant for the case of Berkovich indenters (150 nm) referring to the geometrical features of the specific indenter [62], and R refers to the curvature of the nanoindenter. The penetration depth of the indenter's tip was calculated according to the contact mechanics' analytical expressions (Figure 1) [49,59,63]:

$$h_c = h - h_s = h - \delta\left(\frac{P_{max}}{S}\right),\qquad(5)$$

$$S = \frac{dP}{dh},\qquad(6)$$

where h is the overall displacement of the nanoindenter; δ is a geometric constant parameter referring to the geometrical characteristics of the indenter's tip, which is equal to 0.75 for Berkovich indenters; the variable h_s describes the displacement of the target material's surface during the nanoindentation load, taking into account the pile-up and sink-in deformation mechanisms; and S is the stiffness at the unloading phase. At this point, it is of paramount importance to mention that the stiffness at the unloading step is defined by the incline of the *P-h* diagram (an indicative plot is shown in Figure 2).
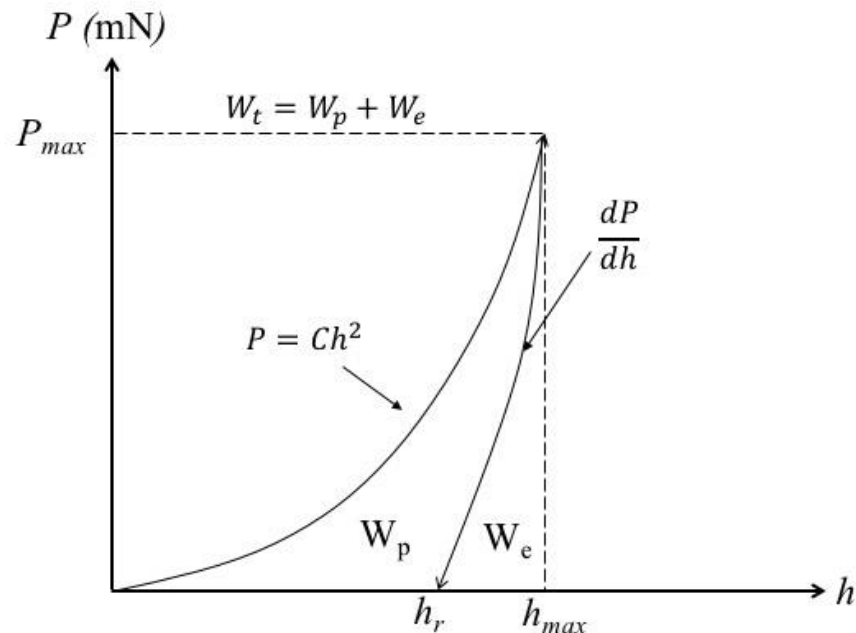

Figure 2. Indentation load–penetration depth curve from an indentation test.

It is noteworthy to mention that Equations (2)–(6) were from research papers in the frame of homogeneous materials. Based on this aspect, extensive work needs to be carried out so as to verify the effectiveness of the proposed mathematical procedure on heterogeneous materials like the nanocrystalline tungsten–copper materials produced and tested in the present paper. The selection of the tungsten–copper alloy was made in the frame of the European FET-Open project ICARUS [64] due to its inherent thermodynamic stability for aerospace applications. Moreover, the strain rate of the indentation at the

surface of the target material is also non-uniform, and it leads to the creation of the corresponding non-uniform stress field, as referred to above. It is of paramount importance to define the mean deformation rate as the rate of the complete penetration depth into the target material over the current total displacement of the indenter [60]:

$$\dot{\varepsilon} = \frac{\dot{h}}{h} \tag{7}$$

2.2. Numerical Model

For the purpose of the nanoindentation simulation of a nanostructured material, a FE-based model was utilized. The recommended numerical methodology is utilized on RVEs with a nanocrystalline morphology. The numerical methodology is presented in the flowchart of Figure 3. The methodology begins with the computer tomograph YXLON FF35 CT (YXLON International GmbH, Hamburg, Germany) and X-ray diffraction images (Bruker D8 Discover, Bruker Corp., Billerica, MA, USA), and evolves with the image analysis and the multi-level simulation [48].
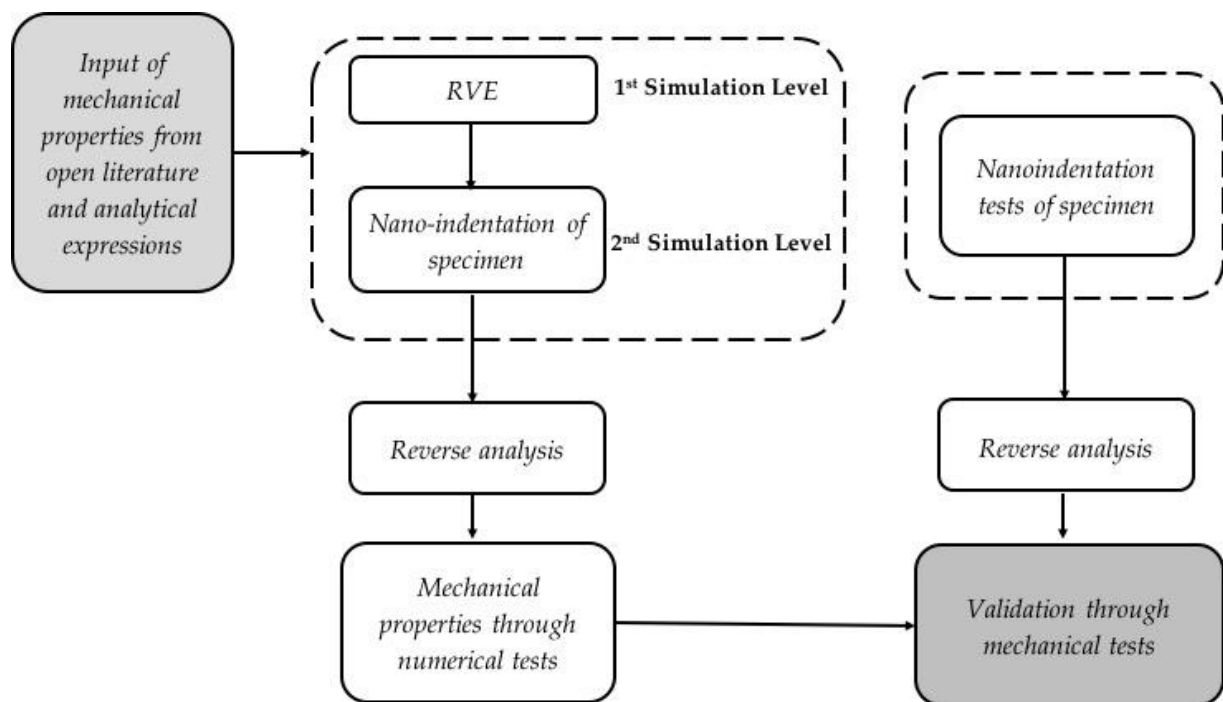

Figure 3. Flowchart of the methodology.

As it is commonly known, RVE is the smallest numerical volume for any material in which a macro-mechanical property can be defined through a multi-scale modelling approach. Due to the microscopic size of representative-volume elements, the detailed morphology of the materials' microstructural characteristics can be modelled. The analysis' objective is focused on the development of a numerical procedure via the parametric interaction representing the geometrical characteristics of nanostructured metals. The presumptions and the extensive numerical methodology used in the present work are described extensively in [48,65], on account of the completeness of the paper. The nanocrystalline materials are heterogeneous materials due to their discrete areas showing different physico-chemical and mechanical properties at the microscale level. Based on this paradox, the mechanical response, taken by the proposed numerical methodology shown in [48,65], is the homogenized average medium of the equivalent heterogenous nanocrystalline material. More specifically, in [48,65], the presumptions were applied for the investigation of mechanical behavior of a fully dense, nanocrystalline material under uniaxial compressive

loading, so as to extract the stress–strain response of an equivalent homogenized material from the heterogenous RVE (see Figure 4) at the nanoscale level under compression loading. In the present publication, we follow strictly the above-said numerical methodology by extending it to the application of a nanoindentation testing method, so as to define the mechanical response of nanocrystalline metals at the microscale level.
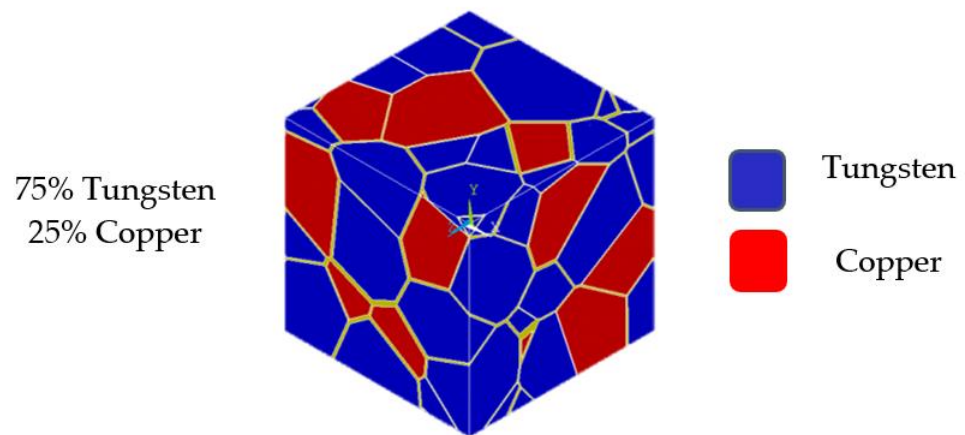

Figure 4. The representative volume element of a tungsten–copper nanocrystalline alloy.

The finite element modeling of the nanoindentation test was developed utilizing Abaqus CAE (Computer Aided Engineering) (Dassault Systemes Simulia Corp., Providence, RI, USA). The model was developed in three dimensions consisting of 2 objects, a representative pyramidal-like indenter with the real dimensions of Berkovich indenter and a cube representing the specimen with dimensions of 5 μm × 5 μm × 3 μm (Figure 5). The indenter was modeled to be rigid. The definition of elastoplastic response of cubic specimen was achieved by using the innovative nanoscale numerical model which was described above [48]. The material properties applied to the cubic specimen were extracted from the RVE as the homogenized average medium. The aforementioned mechanical properties were achieved by applying a compressive loading on the RVE. Additionally, a surface-to-surface frictional contact with a coefficient of 0.1 was implemented for the indentation model. Several numerical investigations have shown that the frictional coefficient between the indenter and target material is an insignificant parameter regarding the experimental nanoindentation outcomes. In the present work, the influence of the frictional contact was taken into account in the numerical model in order to develop numerically the same experimental conditions, with the ultimate goal of the maximum similarity between the numerical model and the experiments. Regarding the numerical parameters, the target material was meshed with 62,000 hexahedral elements of type C3D8R (eight node), with a dense mesh at the area of the target material directly beneath Berkovich's tip. Moreover, the indenter had a constant penetration speed of 5.5 nm/s until it reached the load of 15 mN, in the loading phase, which is a pre-defined setup parameter. After this step, the indenter was removed from the target material with a constant speed of 16 nm/s in the unloading phase. At this point, it is important to mention that the ratio of the cube's height to the maximum penetration depth is approximately equal to 8 in the current model, so as to reduce computational time. From the scope of parametric study, higher ratios of 10 and 20 were also investigated, and the results presented an insignificant divergence in the resulting *P-h* diagram compared to that of the ratio of 8.
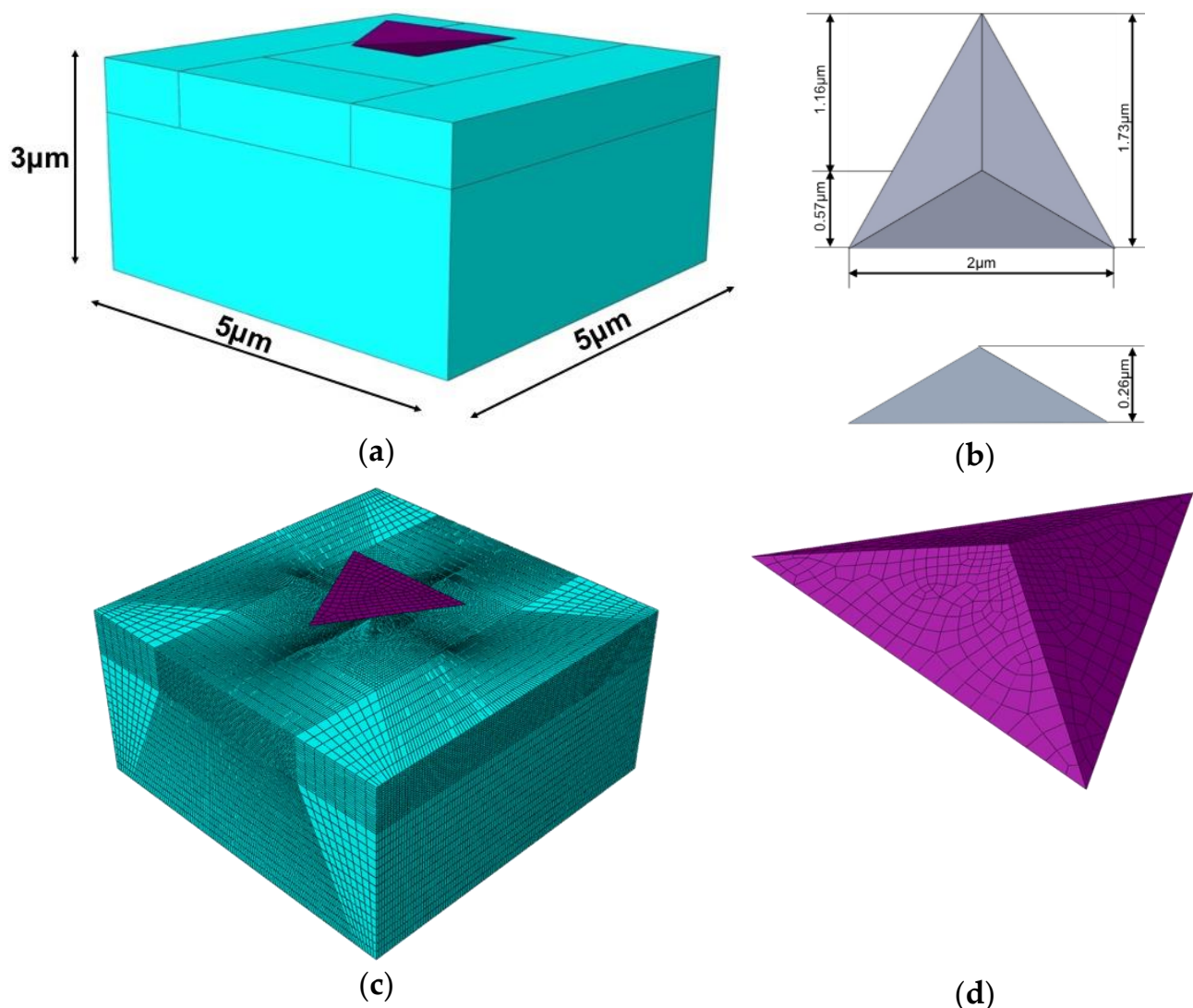
Figure 5. Three-dimensional finite element model of the nanoindentation: (**a**) the dimensions of the target material, (**b**) the dimensions of the Berkovich indenter, (**c**) the meshed model and (**d**) the meshed Berkovich indenter.

The main advantage of the numerical nanoindentation models is that they are able to acquire the load-versus-depth curve of a specified reference point by continuous data acquisition throughout the duration of the simulation, just as during an experiment in situ. Furthermore, another important aspect that should be mentioned is that the proposed numerical methodology has taken into account the importance of the dimensional definition of the indented cube. In this way, the boundary effects are eliminated on the nanoindentation model, and the assumption of a continuous medium was validated. During the setup of the FE parameters, one of the most important boundary conditions applied in this model is the fixation of the target material's base so as to ensure an ideal indentation test. A second important boundary condition applied is the constraint of the nanoindenter in such a way that the nanoindenter is fixed to allow motion in the vertical direction.

2.3. Inverse Analysis Algorithm

A comprehensive analytical methodology for instrumented indentation was identified in this paper, which allows us to define the mechanical properties of materials by using a Berkovich nanoindenter. The current paper is focused on the development of an inverse analysis algorithm so as to obtain the material properties via nanoindentation tests and numerical nanoindentation models. Figure 2 shows the *P-h* curve for a Berkovich indenter.

In the loading phase, it seems that the curve is in consistency with the relation $P = Ch^2$, where parameter C is responsible for the indentation curvature. This curvature represents the resistance of the target material to the indentation effect. Additionally, the calculated pressure of contact, $p_{av} = P_{max}/A_{max}$, could be determined with the hardness of the target material, where P_{max} is the maximum applied force for the indentation. The P_{max} provides the necessary energy to the nanoindenter to penetrate the target material by a depth of h_{max}, by that means creating the A_{max} (the maximum projected contact area on the surface of the target material). Elastoplastic FE models with a Berkovich indenter, conducted on the present paper utilizing computational analyses comparable with those presented in reference [38], also show that

$$\frac{h_r}{h_{max}} = 1 - d^*S, \tag{8}$$

where $d^* = 4.678$ for the case of a Berkovich indenter. Equation (8) is in rational accordance with the experimental observations of Breval and MacMillan [66]. Taking into consideration the true contact area on three-dimensional numerical models and the strain hardening effects imposed on pile-up and sink-in strains, the subsequent mathematical expression, which correlates A_{max} with h_{max}, was obtained for the case study of elastic–plastic materials [30,38]:

$$\frac{A_{max}}{h^2_{max}} = 9.96 - 12.64*(1-S) + 105.42(1-S)^2 - 229.57(1-S)^3 + 157.67(1-S)^4, \; with \; S = \frac{p_{av}}{E^*} \tag{9}$$

The aforementioned mathematical expression is a polynomial regression to the calculated values of A_{max}/h^2_{max}. In Equation (9), the resulting Young's modulus of the Berkovich nanoindenter–target material system, E^*, is derived as:

$$E^* = \frac{1}{c^*\sqrt{A_{max}}}\left(\frac{dP}{dh}\right), \tag{10}$$

where dP/dh is the incline of the P-h diagram at the unloading phase from P_{max}, while the c^* parameter is equal to 1.167 for the case study of the Berkovich nanoindenter. Furthermore, the ratio of the residual penetration depth h_r to the maximum depth of indentation, h_{max}, is typical of the magnitude of strain hardening and plastic deformation [41,67,68]:

$$\frac{\sigma_{0.29} - \sigma_y}{0.29E^*} = 1 - 0.142\frac{h_r}{h_{max}} - 0.957\left(\frac{h_r}{h_{max}}\right)^2 \tag{11}$$

In the aforementioned Equation, σ_y refers to the yield strength, while $\sigma_{0.29}$ refers on the indicative plastic strain of 0.29 for the target material in uniaxial loading.

At this point, it is noteworthy to mention that the combination of Equations (8) and (9) gives an important relationship which correlates A_{max} with h_{max}. Using the aforementioned combined mathematical expression, we are able to extract the true contact area from the P-h diagram without the need of any visual examination. Knowing that

$$P_{max} \approx Ch_{max}^2, \tag{12}$$

we can calculate the parameter C so as to use it into the following equation, which comes from 3D numerical simulations of elastic–plastic nanoindentation, in addition to the corresponding experiments [36,38,42,67,68]:

$$C = \frac{P}{h^2} = M_1\sigma_{0.29}\left\{1 + \frac{\sigma_y}{\sigma_{0.29}}\right\}\left\{M_2 + ln\frac{E^*}{\sigma_y}\right\} \tag{13}$$

The constants in this mathematical expression are M_1 and M_2, where M_1 is equal to 6.618 and M_2 is equal to -0.875 for the case study of a Berkovich indenter [40].

With all of the values calculated using the above-said analytical expressions, the strain hardening exponent can be easily calculated by applying the subsequent equation:

$$n \approx ln\left\{\sigma_{0.29} - \ln\left(\sigma_y\right)\right\}/5 \tag{14}$$

3. Experimental

3.1. Materials

To begin with, the tungsten–copper alloy system was selected for the present investigation. As mentioned above, the selection of the present alloying element combination was made in the frame of the European project ICARUS [64], which was focused on the investigation of coarsening-resistant alloys for aerospace applications. The alloy consisted of 75% tungsten and 25% copper in weight. For this material composition, two different types of tungsten–copper alloy were produced in terms of the resulting microstructure. Both types were manufactured using the same powders originating from the same powder batch.

The coarse-grained tungsten–copper specimens (cW-Cu) were fabricated through the simple mixture of the as-received commercial powders of tungsten and copper elements without any grain refinement process being involved. Additionally, the well-known manufacturing approach consisting of cold pressing, hot isostatic pressing (HIP) (University of Miskolc, Miskolc, Hungary) and heat treatment was implemented so as to obtain the consolidated specimens. The coarse-grained tungsten–copper specimen has an average grain size of 150 nm.

On the other hand, the high energy ball milling (HEBM) (MBN Nanomaterialia S.p.A., Treviso, Italy) method was utilized in order to mill tungsten and copper powders, achieving a nanocrystalline morphology with a grain diameter of 100 nm. The nanocrystalline tungsten–copper powders used for the production of the alloy will be referred in the following as W-Cu. Following the same consolidation technique of the cW-Cu specimens for the production of the corresponding W-Cu specimens, the fabrication method of cold pressing, hot isostatic pressing (HIP) and heat treatment was implemented here again. An extensive description of the produced materials' microstructures and their resulting imperfections (pores and impurities) can be found in [48]. The above-mentioned production of the two types of tungsten–copper alloys was performed by the company MBN Nanomaterialia.

3.2. Nanoindentation Test

Nanoindentation refers to a variety of hardness tests which are applied on a small scale. Penetration is perhaps the most common way of checking the mechanical properties of materials facilitated by high-precision instrumentation in the nanometer scale. In 2008, the ISO/TR 29381 was published, allowing for the evaluation of the tensile properties of metallic materials by instrumented indentation [69].

A nanoindentation device was developed at the Physical Metallurgy Laboratory, and is presented in Figures 6 and 7. The device performs testing using a Berkovich, Vickers, or Knoop diamond, or 0.5–2 mm indenters. The travel distance of the workbench can reach 50 by 140 mm, guided by specially developed computer software. The height of the optics is measured by means of a laser distance meter coupled with a rotary encoder attached to the fine adjustment dial of the microscope. The accuracy of the device in the XY direction is in the order of 1 μm. The applied load can vary from 1 to 1000 mN with a resolution of 0.1 mN, strictly following the ISO 14577 [70]. The measurement consists of two stages: the loading phase and the unloading phase. During the loading, force is applied gradually to the diamond indenter, and as it penetrates the test piece, the depth measurement is recorded. During the unloading, a residual depth remains due to the plastic deformation of the sample, which depends on the properties of the material, the size of the applied force, and the geometry of the indenter. The maximum indentation depth fluctuations measured on the same sample are mainly induced by different contact conditions between the indenter tip and the tested surface due to roughness [71]. The roughness effect can be confronted with the execution of an appreciable number of measurements to attain the stabilization of

the maximum indentation depth's mean value [71]. The proper preparation of the examined specimens is a meticulous and time-consuming process that ensures the repeatability and robustness of the results, while eliminating those parameters that could tamper with the outcome due to mishandling or human error. The mounted samples were gently, mechanically ground and polished in several sequential steps employing a BUEHLER Vanguard^{TM} 2000 (Lake Bluff, IL, USA) automatic sample preparation system [72]. The mechanical grinding took place in several sequential steps, starting with coarse grinding discs (60 grit) and ending with finer ones (1600 grit). The polishing was obtained by employing an aqueous suspension of fine alumina powder with a particle size of 0.3 μm applied on the respective polishing cloths. In this work, 50 nanoindentation tests were performed on each specimen to eliminate roughness effects.

Figure 6. Nanoindentation test of nanocrystalline specimens according to ISO 14577.
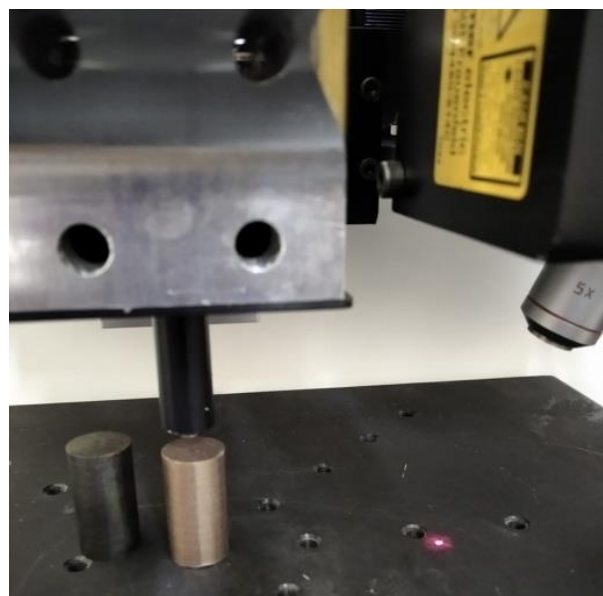

Figure 7. Specimen's fixation for the nanoindentation test.

The evolution of FEM-based algorithms in the evaluation of nanoindentation results offers advanced capabilities in the determination of the exact contact between the indenter and the test piece, thus allowing the accurate calculation of the material's hardness and the stress–strain curve. The FEM model simulating the nanoindentation procedure and the actual indenter tip geometry, introduced in [72], can be applied to calculate the contact geometry during the loading and the shape of the surface impression after unloading. The

"SSCUBONI" algorithm employed for the continuous simulation of the nanoindentation enables the extraction of materials' stress–strain laws. FEM-supported methods offer advanced capabilities in the determination of mechanical properties, such as the Young's modulus, yield and rupture strength. Stress–strain curves of various materials—such as cemented carbide, ceramics and hardened steels—determined by a FEM-based algorithm of nanoindentation can be applied in FEM-supported simulations of micro- and macro-scale indentation procedures to allow the capture of the material response at various scales [73].

4. Results

The indentation force (*P*)–penetration depth (*h*) curves obtained using a Berkovich indenter tip, after a set of 50 measurements that were statistically evaluated to present the averages for the cW-Cu and the W-Cu type of alloy are presented in Figure 8, as well as the scatter of the measurement at the maximum indentation depth. As shown in Figure 8, the coarse-grained tungsten–copper alloy (cW-Cu) exhibits a higher penetration of about 400nm depth at an indentation load of 15 mN [73,74] compared to that of nanocrystalline the tungsten–copper alloy (W-Cu), which presents a penetration depth of about 250 nm at the applied penetration load of 15 mN, correspondingly. The aforementioned outcomes are reasonable due to the fact that the Hall–Petch effect governs this type of material, and the yield stress is increased by decreasing the grain size. Thus, the nanocrystalline specimen shows a higher "resistance" to the indentation effect and to plastic deformation.
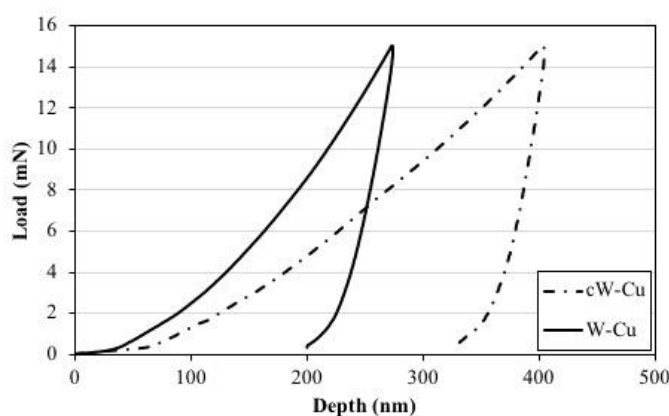
	cW-cu	W-cu
Min. Depth (nm)	352	224
Aver. Depth (nm)	407	258
Max. depth (nm)	522	284

(**a**)　　　　　　　　　　　　　　　　　　　　　　　　　(**b**)

Figure 8. (**a**) The experimental results of cW-Cu and WCu specimens in accordance with ISO 14577, and (**b**) the scatter of the nanoindentation results.

4.1. Validation of the Numerical Nanoindentation Model

Using the numerical multiscale model, the homogenized nanoindentation response of the fully dense, indented material was calculated for the case of a coarse-grained W-Cu (cW-Cu) material, and is shown in Figure 9. In this Figure, the computed *P-h* curves of a fully dense, nanocrystalline material using two Berkovich indenters—one with a sharp tip and one with a rounded tip with a roundness of 100 nm—are displayed and compared to the respective experimental curve. The geometrical features and the material properties applied on the cubic specimen are described extensively in [48]. The divergence of the numerical outcomes from the experimental result is negligible because the nanoindentation model does not take into account any defect (like pores) which might be located in the microstructure of the specimens. The aforementioned assumption of the absence of defects on the numerical model leads to the simulation of a fully dense, homogeneous-like material which may be different from that reality. On the other hand, the existing impurities or pores are mostly located at the lower layers of specimens, and as a result the nanoindenter cannot reach it through the nanoindentation test due to the very small indentation depth.

This phenomenon leads to the prediction of a nanoindentation response of a fully dense material without microstructure irregularities.
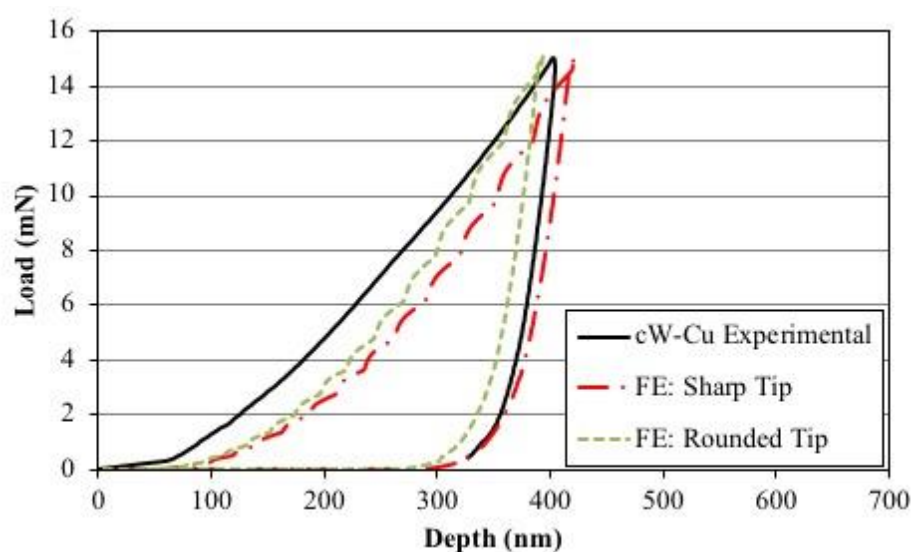

Figure 9. Comparison of the experimental result of the cW-Cu specimen with the numerical results utilizing sharp and rounded Berkovich indenters.

Taking for granted the above assumption, the only parameter which plays an important role on the definition of the nanoindentation response is the sharpness of the nanoindenter. In terms of the tip sharpness, both the tungsten–copper alloys and their corresponding numerical results (Figures 9 and 10) present the same tendency. More specifically, the numerical results of the sharp Berkovich indenter present the higher penetration depth of both materials. This phenomenon is reasonable due to the extensive stress concentration beneath the Berkovich tip. The sharper the tip, the higher the stress concentration factor is. On the other hand, the implementation of a rounded tip of the Berkovich indenter is a more realistic approach due to the unavoidable degeneration of the nanoindentation apparatus through its extensive usage. The above fact is logical, and the effect of the indenter's sharpness on the mechanical response in nanoindentation experiment was reported in [75]. Taking this aspect for granted, the numerical results of the rounded Berkovich indenter tend to show the most reliable nanoindentation behavior.
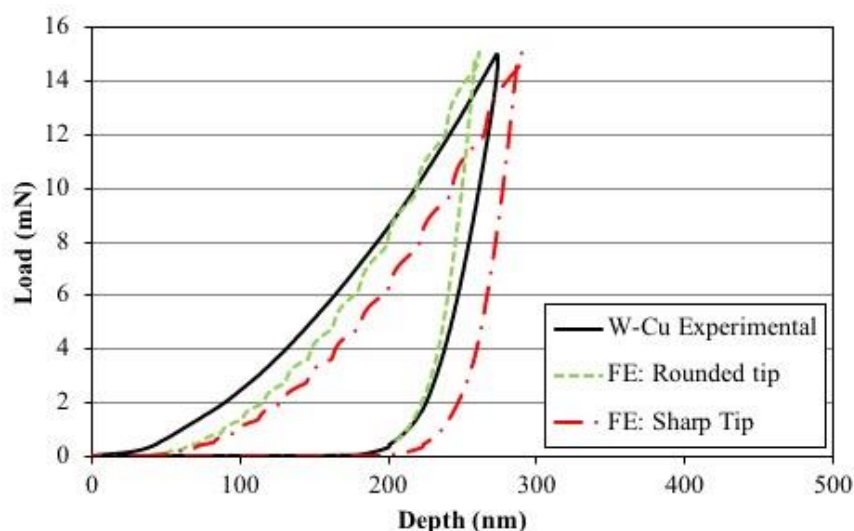

Figure 10. Comparison of the experimental result of a W-Cu specimen with the numerical results of a fully dense model utilizing sharp and rounded Berkovich indenters.

To sum up, the experimental *P-h* curve better reflects the nanoindentation behavior of a fully dense material than of a material with an extensive porosity like the examined specimens in this paper. The proposed numerical methodology shows a very good convergence with the nanoindentation test. On the other hand, utilizing the inverse algorithm as it is shown in Section 4.2, the macroscopic compression behavior obtained by the inverse algorithm of the numerical nanonindentation results will differ from the experimental compression tests examined in [48] because it does not take into account the inherent defects (impurities and pores) of the microstructure.

4.2. Comparison of Nanoindentation Experimental Results Utilizing the SSCUBONI Algorithm

Implementing the SSCUBONI algorithm, the resulting representative von Mises stress–strain curves of the cW-Cu and W-Cu specimens from the nanoindentation tests are shown in Figures 11 and 12, respectively. The aforementioned curves are compared to those of the compression tests for the same batches.
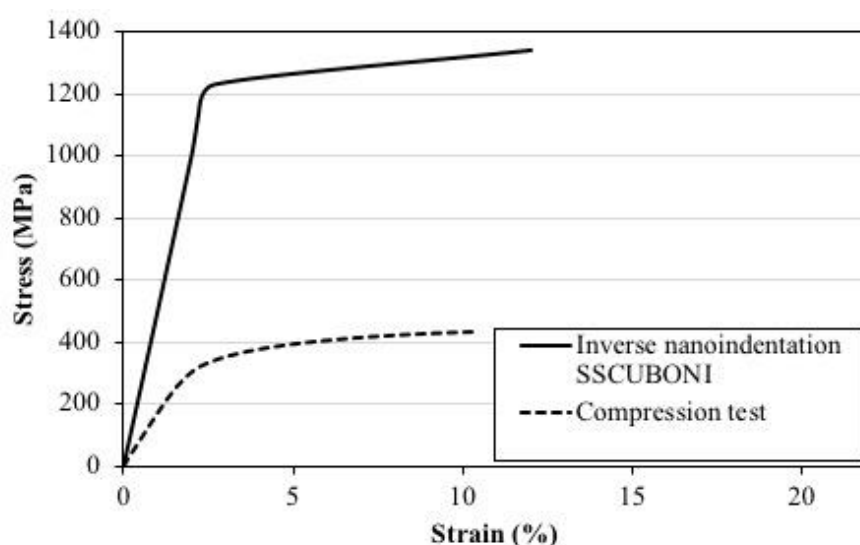

Figure 11. Comparison of the S-S curves of the experimental compression test with the corresponding inverse SSCUBONI-based experimental test for the cW-Cu specimens.
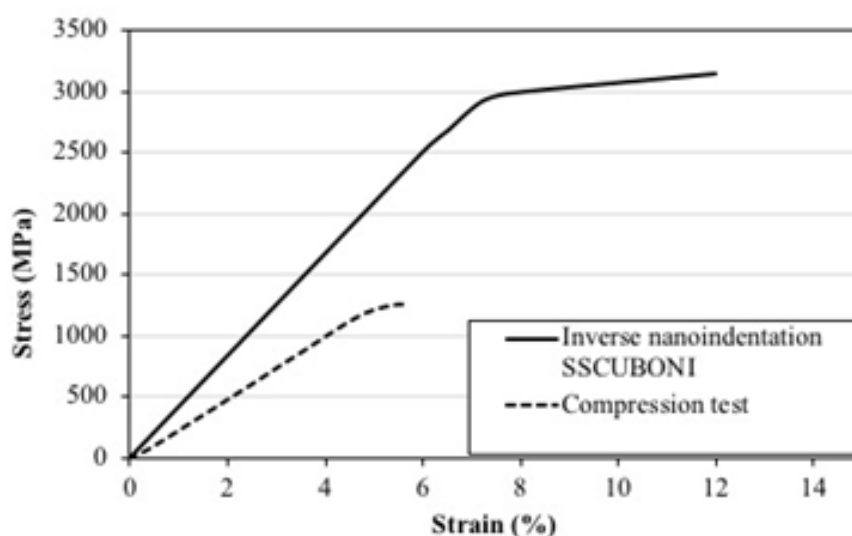

Figure 12. Comparison of the S-S curves of the experimental compression test with the corresponding inverse SSCUBONI-based experimental test for the W-Cu specimens.

As can be seen from both Figures, the inverse experimental nanoindentation results present a remarkable deviation from the compression test of the cW-Cu and W-Cu counterparts. More specifically, in Figure 11, the inverse SSCUBONI nanoindentation curve exhibits a Young's modulus of 200 GPa and a yield stress of 1340 MPa, while the corresponding compression curve shows a Young's modulus of 180 GPa and a yield stress of 450 MPa. Moreover, in the case of W-Cu specimens (Figure 12), the inverse SSCUBONI curve from the experimental nanoindentation curve shows a Young's modulus of 250 GPa and a yield stress of 2.8 GPa, while the respective compression curve for the case of the W-Cu specimen exhibits a Young's modulus of 220 GPa and a yield stress of 1150 MPa.

It is evident that the deviation of the inverse experimental nanoindentation outcomes from the experimental compression results is appreciable but reasonable. The porosity effect is the main characteristic which relies on the aforementioned deviation. As was already explained above, the nanoindenter penetrates the target material at a contact area of a few nanometers for an indentation depth of some nanometers. The contact area of the nanoindentation is extremely small compared to the volume of the specimen, and as a result the obtained experimental results reflect a nanoindentation behavior of a homogeneous-like material excluding all of the present heterogeneities into its microstructure by extracting a nanoindentation behavior of an ideal material. This procedure leads to unreliable results in the case of a material with several defects or impurities in its microstructure. The experimental test is not able to perceive the extensive presence of pores which are located in the lower layers. In our case, the experimental *P-h* curve better reflects the nanoindentation behaviour of a fully dense material than that of a material with an extensive porosity like the examined specimens of the current project.

4.3. Comparison of Numerical Nanoindentation Results Utilizing the Inverse Algorithm

In an effort to predict the macroscopic material properties via the nanoindentation testing method, an inverse algorithm was proposed and utilized in this paper. The macroscopic mechanical responses of the experimental results and the numerical outcomes of nanoindentation models were calculated for the case of a cW-Cu material and a W-Cu material, and they are shown in Figures 13 and 14, respectively. As can be seen, the experimental nanoindentation results obtained from the SSCUBONI algorithm show an appreciable convergence with the corresponding numerical nanoindentation results obtained by the proposed inverse algorithm.
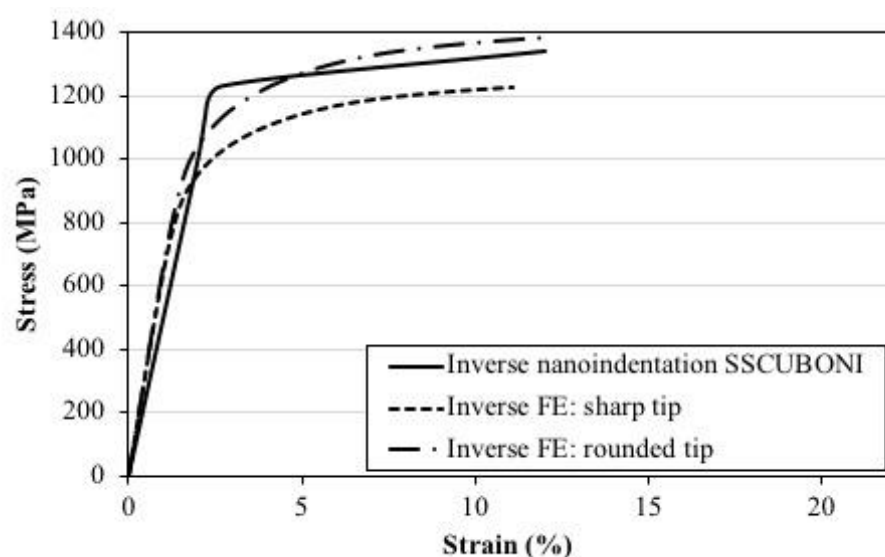

Figure 13. Comparison of the S-S curves of the experimental compression test with the corresponding inverse numerical nanoindentation results and the inverse SSCUBONI-based experimental test for the cW-Cu specimens.
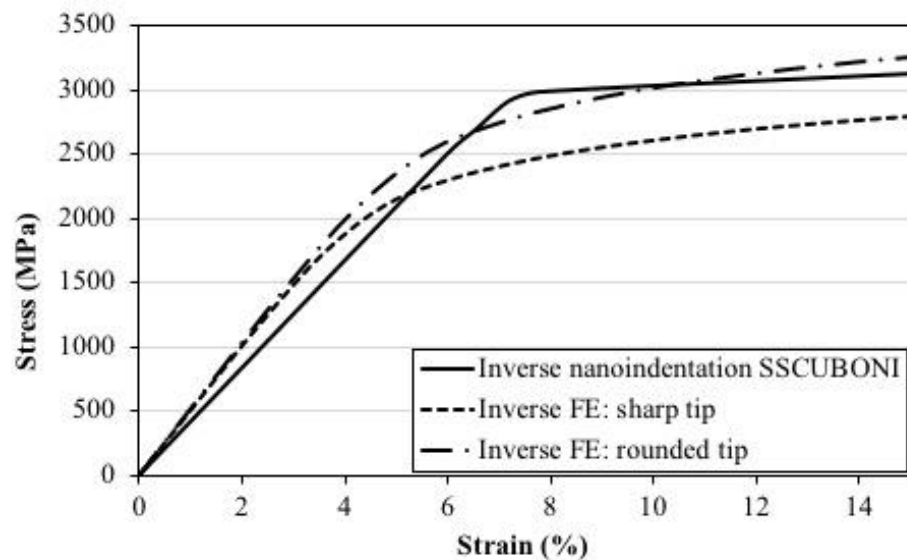
Figure 14. Comparison of the S-S curves of the experimental compression test with the corresponding inverse numerical nanoindentation results and the inverse SSCUBONI-based experimental test for the W-Cu specimens.

Both of the inverse analysis algorithms seem to be efficient in converting the penetration load–indentation depth curve to stress–strain curves, but the proposed multiscale nanoindentation model in conjunction with the inverse algorithm provides an advantage to the scientific community because it is able to predict the macroscopic mechanical response of any nanocrystalline material without executing any experimental test. However, it is noteworthy to mentioned at this point that the porosity effect is a crucial parameter for the mechanical behavior. For the aforementioned reason, the numerical multiscale nanoindentation methodology implementing the porosity effect for the case study of porous nanocrystalline alloys in combination with the proposed inverse analysis algorithm needs to be developed so as to predict the macroscopic mechanical response more efficiently.

5. Conclusions

Herein, a methodology was developed for the simulation of the nanoindentation testing of fully dense nanocrystalline materials utilizing a combination of numerical and analytical approaches. The numerical nanoindentation outcomes correlate very well with the experimental nanoindentation results, which validates the proposed methodology in terms of simulating the nanoindentation test. However, in the scope of the prediction of mechanical properties at the macroscale level, the proposed methodology shows an appreciable divergence with the experimental compression tests due to the porosity effect. For the aforementioned reason, it is of paramount importance that the proposed multiscale numerical methodology be modified so as to take into account the porosity effect. Additionally, a thorough investigation of the proposed methodology has to be carried out by applying different indentation loads, through numerical simulations and experimental tests, and by testing various specimens with different alloying elements, compositions and grain sizes so as to be validated for any alloy. Considering the above, it can be stated that the proposed numerical approach in conjunction with the inverse algorithm represents a preliminary contribution towards the development of a numerical nanoindentation model, and may serve as the basis for the development of large-scale models to be applied in the quality control of the mass production systems of the aforementioned promising materials in the near future.

References

1. Gleiter, H. Nanostructured materials: Basic concepts and microstructure. *Acta Mater.* **2000**, *48*, 1–29. [CrossRef]
2. Kumar, K.; Van Swygenhoven, H.; Suresh, S. Mechanical behavior of nanocrystalline metals and alloys The Golden Jubilee Issue—Selected topics in Materials Science and Engineering: Past, Present and Future, edited by S. Suresh. *Acta Mater.* **2003**, *51*, 5743–5774. [CrossRef]
3. Naik, S.; Walley, S. The Hall–Petch and inverse Hall–Petch relations and the hardness of nanocrystalline metals. *J. Mater. Sci.* **2019**, *55*, 2661–2681. [CrossRef]
4. Hibbard, G.; Erb, U.; Aust, K.; Klement, U.; Palumbo, G. Thermal Stability of Nanostructured Electrodeposits. *J. Metastable Nanocryst. Mater.* **2002**, *13*, 387–396. [CrossRef]
5. Suryanarayana, C. Nanocrystalline materials. *Int. Mater. Rev.* **1995**, *40*, 41–64. [CrossRef]
6. Groza, J. Nanostructured Materials. *Mater. Today* **2002**, *5*, 55.
7. Liao, W.; Lan, S.; Gao, L.; Zhang, H.; Xu, S.; Song, J.; Wang, X.; Lu, Y. Nanocrystalline high-entropy alloy (CoCrFeNiAl0.3) thin-film coating by magnetron sputtering. *Thin Solid Films* **2017**, *638*, 383–388. [CrossRef]
8. Liao, W.; Zhang, H.; Liu, Z.; Li, P.; Huang, J.; Yu, C.; Lu, Y. High Strength and Deformation Mechanisms of Al0.3CoCrFeNi High-Entropy Alloy Thin Films Fabricated by Magnetron Sputtering. *Entropy* **2019**, *21*, 146. [CrossRef] [PubMed]
9. Xing, Q.; Ma, J.; Zhang, Y. Phase thermal stability and mechanical properties analyses of (Cr,Fe,V)-(Ta,W) multiple-based elemental system using a compositional gradient film. *Int. J. Miner. Metall. Mater.* **2020**, *27*, 1379–1387. [CrossRef]
10. Xing, Q.; Ma, J.; Wang, C.; Zhang, Y. High-Throughput Screening Solar-Thermal Conversion Films in a Pseudobinary (Cr, Fe, V)-(Ta, W) System. *ACS Comb. Sci.* **2018**, *20*, 602–610. [CrossRef]
11. Lowe, T.; Valiev, R. Producing nanoscale microstructures through severe plastic deformation. *JOM* **2000**, *52*, 27–28. [CrossRef]
12. Valiev, R.; Islamgaliev, R.; Alexandrov, I. Bulk nanostructured materials from severe plastic deformation. *Prog. Mater. Sci.* **2000**, *45*, 103–189. [CrossRef]
13. Zhou, H.; Hu, L.; Sun, Y.; Zhang, H.; Duan, C.; Yu, H. Synthesis of nanocrystalline AZ31 magnesium alloy with titanium addition by mechanical milling. *Mater. Charact.* **2016**, *113*, 108–116. [CrossRef]
14. Suresh, S. Graded Materials for Resistance to Contact Deformation and Damage. *Science* **2001**, *292*, 2447–2451. [CrossRef]
15. Delfosse, D. Fundamentals of Functionally Graded Materials. *Mater. Today* **1998**, *1*, 18. [CrossRef]
16. Masumura, R.; Hazzledine, P.; Pande, C. Yield stress of fine grained materials. *Acta Mater.* **1998**, *46*, 4527–4534. [CrossRef]
17. Jeong, D.; Gonzalez, F.; Palumbo, G.; Aust, K.; Erb, U. The effect of grain size on the wear properties of electrodeposited nanocrystalline nickel coatings. *Scr. Mater.* **2001**, *44*, 493–499. [CrossRef]
18. Hayes, R.; Witkin, D.; Zhou, F.; Lavernia, E. Deformation and activation volumes of cryomilled ultrafine-grained aluminum. *Acta Mater.* **2004**, *52*, 4259–4271. [CrossRef]
19. Jia, D.; Ramesh, K.; Ma, E. Effects of nanocrystalline and ultrafine grain sizes on constitutive behavior and shear bands in iron. *Acta Mater.* **2003**, *51*, 3495–3509. [CrossRef]
20. Cavaliere, P. Strain Rate Sensitivity and Fatigue Properties of an Al-fe Nanocrystalline Alloy Produced by Cryogenic Ball Milling. *Multidiscip. Model. Mater. Struct.* **2007**, *3*, 225–234. [CrossRef]
21. Tabor, D. *The Hardness of Metals*; Oxford University Press: New York, NY, USA, 1951.
22. Tabor, D. The hardness of solids. *Rev. Phys. Technol.* **1970**, *1*, 145–179. [CrossRef]
23. Doerner, M.; Nix, W. A method for interpreting the data from depth-sensing indentation instruments. *J. Mater. Res.* **1986**, *1*, 601–609. [CrossRef]
24. Pharr, G.; Cook, R. Instrumentation of a conventional hardness tester for load-displacement measurement during indentation. *J. Mater. Res.* **1990**, *5*, 847–851. [CrossRef]

25. Oliver, W.; Pharr, G. An improved technique for determining hardness and elastic modulus using load and displacement sensing indentation experiments. *J. Mater. Res.* **1992**, *7*, 1564–1583. [CrossRef]
26. Field, J.; Swain, M. A simple predictive model for spherical indentation. *J. Mater. Res.* **1993**, *8*, 297–306. [CrossRef]
27. Field, J.; Swain, M. Determining the mechanical properties of small volumes of material from submicrometer spherical indentations. *J. Mater. Res.* **1995**, *10*, 101–112. [CrossRef]
28. Gerberich, W.; Nelson, J.; Lilleodden, E.; Anderson, P.; Wyrobek, J. Indentation induced dislocation nucleation: The initial yield point. *Acta Mater.* **1996**, *44*, 3585–3598. [CrossRef]
29. Bolshakov, A.; Oliver, W.; Pharr, G. Influences of stress on the measurement of mechanical properties using nanoindentation: Part II. Finite element simulations. *J. Mater. Res.* **1996**, *11*, 760–768. [CrossRef]
30. Alcalá, J.; Giannakopoulos, A.; Suresh, S. Continuous measurements of load-penetration curves with spherical microindenters and the estimation of mechanical properties. *J. Mater. Res.* **1998**, *13*, 1390–1400. [CrossRef]
31. Cheng, Y.; Cheng, C. Scaling approach to conical indentation in elastic-plastic solids with work hardening. *J. Appl. Phys.* **1998**, *84*, 1284–1291. [CrossRef]
32. Cheng, Y.; Cheng, C. Relationships between hardness, elastic modulus, and the work of indentation. *Appl. Phys. Lett.* **1998**, *73*, 614–616. [CrossRef]
33. Suresh, S.; Nieh, T.; Choi, B. Nano-indentation of copper thin films on silicon substrates. *Scr. Mater.* **1999**, *41*, 951–957. [CrossRef]
34. Gouldstone, A.; Koh, H.; Zeng, K.; Giannakopoulos, A.; Suresh, S. Discrete and continuous deformation during nanoindentation of thin films. *Acta Mater.* **2000**, *48*, 2277–2295. [CrossRef]
35. Johnson, K. The correlation of indentation experiments. *J. Mech. Phys. Solids* **1970**, *18*, 115–126. [CrossRef]
36. Suresh, S.; Alcala, J.; Giannakopoulos, A. Depth Sensing Indentation and Methodology for Mechanical Property Measurements. U.S. Patent 6134954A, 19 June 2020.
37. Dao, M.; Chollacoop, N.; Van Vliet, K.; Venkatesh, T.; Suresh, S. Computational modeling of the forward and reverse problems in instrumented sharp indentation. *Acta Mater.* **2001**, *49*, 3899–3918. [CrossRef]
38. Giannakopoulos, A.; Larsson, P.; Vestergaard, R. Analysis of Vickers indentation. *Int. J. Solids Struct.* **1994**, *31*, 2679–2708. [CrossRef]
39. Cheng, Y.; Cheng, C. Can stress–strain relationships be obtained from indentation curves using conical and pyramidal indenters? *J. Mater. Res.* **1999**, *14*, 3493–3496. [CrossRef]
40. Giannakopoulos, A.; Suresh, S. Determination of elastoplastic properties by instrumented sharp indentation. *Scr. Mater.* **1999**, *40*, 1191–1198. [CrossRef]
41. Venkatesh, T. Determination of elasto-plastic properties by instrumented sharp indentation: Guidelines for property extraction. *Scr. Mater.* **2000**, *42*, 833–839. [CrossRef]
42. Suresh, S.; Giannakopoulos, A. A new method for estimating residual stresses by instrumented sharp indentation. *Acta Mater.* **1998**, *46*, 5755–5767. [CrossRef]
43. Bhattacharya, A.; Nix, W. Finite element simulation of indentation experiments. *Int. J. Solids Struct.* **1988**, *24*, 881–891. [CrossRef]
44. Laursen, T.; Simo, J. A study of the mechanics of microindentation using finite elements. *J. Mater. Res.* **1992**, *7*, 618–626. [CrossRef]
45. Tunvisut, K.; O'Dowd, N.; Busso, E. Use of scaling functions to determine mechanical properties of thin coatings from microindentation tests. *Int. J. Solids Struct.* **2001**, *38*, 335–351. [CrossRef]
46. Hill, R.; Storakers, B.; Zdunek, A. A theoretical study of the Brinell hardness test. *Proc. R. Soc. Lond. A Math. Phys. Sci.* **1989**, *423*, 301–330.
47. Larsson, P.; Giannakopoulos, A.; SÖderlund, E.; Rowcliffe, D.; Vestergaard, R. Analysis of Berkovich indentation. *Int. J. Solids Struct.* **1996**, *33*, 221–248. [CrossRef]
48. Bazios, P.; Tserpes, K.; Pantelakis, S. Modelling and Experimental Validation of the Porosity Effect on the Behaviour of Nano-Crystalline Materials. *Metals* **2020**, *10*, 821. [CrossRef]
49. Oliver, W.; Pharr, G. Measurement of hardness and elastic modulus by instrumented indentation: Advances in understanding and refinements to methodology. *J. Mater. Res.* **2004**, *19*, 3–20. [CrossRef]
50. Chrobak, D.; Kim, K.; Kurzydłowski, K.; Nowak, R. Nanoindentation experiments with different loading rate distinguish the mechanism of incipient plasticity. *Appl. Phys. Lett.* **2013**, *103*, 072101. [CrossRef]
51. Wang, Y.; Raabe, D.; Klüber, C.; Roters, F. Orientation dependence of nanoindentation pile-up patterns and of nanoindentation microtextures in copper single crystals. *Acta Mater.* **2004**, *52*, 2229–2238. [CrossRef]
52. Tadmor, E.; Miller, R.; Phillips, R.; Ortiz, M. Nanoindentation and incipient plasticity. *J. Mater. Res.* **1999**, *14*, 2233–2250. [CrossRef]
53. Zhang, J.; Zhang, J.; Wang, Z.; Hartmaier, A.; Yan, Y.; Sun, T. Interaction between phase transformations and dislocations at incipient plasticity of monocrystalline silicon under nanoindentation. *Comput. Mater. Sci.* **2017**, *131*, 55–61. [CrossRef]
54. Fischer-Cripps, A. A simple phenomenological approach to nanoindentation creep. *Mater. Sci. Eng. A* **2004**, *385*, 74–82. [CrossRef]
55. Elmustafa, A.; Stone, D. Nanoindentation and the indentation size effect: Kinetics of deformation and strain gradient plasticity. *J. Mech. Phys. Solids* **2003**, *51*, 357–381. [CrossRef]
56. Karthik, V.; Visweswaran, P.; Bhushan, A.; Pawaskar, D.; Kasiviswanathan, K.; Jayakumar, T.; Raj, B. Finite element analysis of spherical indentation to study pile-up/sink-in phenomena in steels and experimental validation. *Int. J. Mech. Sci.* **2012**, *54*, 74–83. [CrossRef]

57. Biener, M.; Biener, J.; Hodge, A.; Hamza, A. Dislocation nucleation in bcc Ta single crystals studied by nanoindentation. *Phys. Rev. B* **2007**, *76*, 165422. [CrossRef]

58. Morris, J.; Bei, H.; Pharr, G.; George, E. Size Effects and Stochastic Behavior of Nanoindentation Pop In. *Phys. Rev. Lett.* **2011**, *106*. [CrossRef]

59. Hasnine, M.; Mustafa, M.; Suhling, J.; Prorok, B.; Bozack, M.; Lall, P. Characterization of aging effects in lead free solder joints using nanoindentation. In Proceedings of the 2013 IEEE 63rd Electronic Components and Technology Conference, Las Vegas, NV, USA, 28–31 May 2013; pp. 166–178. [CrossRef]

60. Lucas, B.; Oliver, W. Indentation power-law creep of high-purity indium. *Metall. Mater. Trans. A* **1999**, *30*, 601–610. [CrossRef]

61. Zhang, P.; Li, S.; Zhang, Z. General relationship between strength and hardness. *Mater. Sci. Eng. A* **2011**, *529*, 62–73. [CrossRef]

62. Hay, J.; Agee, P.; Herbert, E. Continuous stiffness measurement during instrumented indentation testing. *Exp. Tech.* **2010**, *34*, 86–94. [CrossRef]

63. Chen, X.; Xiang, Y.; Vlassak, J. Novel technique for measuring the mechanical properties of porous materials by nanoindentation. *J. Mater. Res.* **2006**, *21*, 715–724. [CrossRef]

64. Innovative Coarsening-Resistant Alloys with Enhanced Radiation Tolerance and Ultrafine-Grained Structure for Aerospace Application|ICARUS. Available online: http://icarus-alloys.eu (accessed on 14 June 2020).

65. Bazios, P.; Tserpes, K.; Pantelakis, S. Numerical Computation of Material Properties of Nanocrystalline Materials Utilizing Three-Dimensional Voronoi Models. *Metals* **2019**, *9*, 202. [CrossRef]

66. Breval, E.; Macmillan, N. Elastic recovery at Vickers hardness impressions. *J. Mater. Sci. Lett.* **1985**, *4*, 741–742. [CrossRef]

67. Suresh, S.; Giannakopoulos, A.; Alcalá, J. Spherical indentation of compositionally graded materials: Theory and experiments. *Acta Mater.* **1997**, *45*, 1307–1321. [CrossRef]

68. Suresh, S.A.; Giannakopoulos, A. *Report Inst-2/98*; Massachusetts Institute of Technology: Cambridge, MA, USA, 1998.

69. ISO/TR 29381. *Metallic Materials—Measurement of Mechanical Properties by an Instrumented Indentation Test—Indentation Tensile Properties*; ISO: Geneva, Switzerland, 2008.

70. ISO 14577. *Metallic Materials–Instrumented Indentation Test for Hardness and Materials Parameters, Part 1: Test Method, 2002, Part 2: Verification and Calibration of Testing Machines, 2002, Part 3: Calibration of Reference Blocks, 2002, Part 4: Test Method for Metallic and Non-Metallic Coatings*; ISO: Geneva, Switzerland, 2007.

71. Bouzakis, K.; Michailidis, N.; Hadjiyiannis, S.; Skordaris, G.; Erkens, G. The effect of specimen roughness and indenter tip geometry on the determination accuracy of thin hard coatings stress–strain laws by nanoindentation. *Mater. Charact.* **2002**, *49*, 149–156. [CrossRef]

72. Available online: http://www.horizonindia.in/buehler/grinders-polishers/3-BUEHLERVANGUARD.pdf (accessed on 31 October 2021).

73. Michailidis, N.; Pappa, M. Application of strength properties determined by nanoindentations to describe the material response in micro- and macro-indentation. *CIRP Ann.* **2009**, *58*, 511–514. [CrossRef]

74. Michailidis, N.; Bouzakis, K.; Koenders, L.; Herrmann, K. *Nanoindentation, CIRP Encyclopedia of Production Engineering*; Springer: Berlin/Heidelberg, Germany, 2014; pp. 1–9.

75. Lichinchi, M.; Lenardi, C.; Haupt, J.; Vitali, R. Simulation of Berkovich nanoindentation experiments on thin films using finite element method. *Thin Solid Films* **1998**, *312*, 240–248. [CrossRef]